ACS APPLIED MATERIALS & INTERFACES

www.acsami.org

Research Article

Au-Decorated Ce–Ti Mixed Oxides for Efficient CO Preferential Photooxidation

Antonia Infantes-Molina, Andrea Villanova, Aldo Talon, Mojtaba Gilzad Kohan, Alessandro Gradone, Raffaello Mazzaro, Vittorio Morandi, Alberto Vomiero,* and Elisa Moretti*

Cite This: *ACS Appl. Mater. Interfaces* 2020, 12, 38019–38030

Read Online

ACCESS | Metrics & More | Article Recommendations | Supporting Information

ABSTRACT: We investigated the photocatalytic behavior of gold nanoparticles supported on CeO_2–TiO_2 nanostructured matrixes in the CO preferential oxidation in H_2-rich stream (photo-CO-PROX), by modifying the electronic band structure of ceria through addition of titania and making it more suitable for interacting with free electrons excited in gold nanoparticles through surface plasmon resonance. CeO_2 samples with different TiO_2 concentrations (0–20 wt %) were prepared through a slow coprecipitation method in alkaline conditions. The synthetic route is surfactant-free and environmentally friendly. Au nanoparticles (<1.0 wt % loading) were deposited on the surface of the CeO_2–TiO_2 oxides by deposition–precipitation. A benchmarking sample was also considered, prepared by standard fast coprecipitation, to assess how a peculiar morphology can affect the photocatalytic behavior. The samples appeared organized in a hierarchical needle-like structure, with different morphologies depending on the Ti content and preparation method, with homogeneously distributed Au nanoparticles decorating the Ce–Ti mixed oxides. The morphology influences the preferential photooxidation of CO to CO_2 in excess of H_2 under simulated solar light irradiation at room temperature and atmospheric pressure. The Au/CeO_2–TiO_2 systems exhibit much higher activity compared to a benchmark sample with a non-organized structure. The most efficient sample exhibited CO conversions of 52.9 and 80.2%, and CO_2 selectivities equal to 95.3 and 59.4%, in the dark and under simulated sunlight, respectively. A clear morphology–functionality correlation was found in our systematic analysis, with CO conversion maximized for a TiO_2 content equal to 15 wt %. The outcomes of this study are significant advancements toward the development of an effective strategy for exploitation of hydrogen as a viable clean fuel in stationary, automotive, and portable power generators.

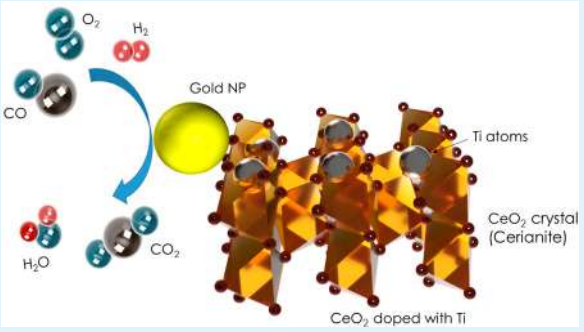

KEYWORDS: *CO preferential oxidation, CO-PROX, ceria–titania, gold nanoparticles, photocatalysis*

INTRODUCTION

Over past decades, the environmental issues related to the use of non-renewable energy sources, the massive emission of greenhouse gases and the exponential growth of world energy consumption, have been fostering the research on renewable and environmentally friendly energy sources. Among the many different strategies developed, hydrogen has turned out to be the ideal clean energy carrier,[1] since it can be employed as feedstock in fuel cells,[2] among which are low temperature polymer electrolyte fuel cells (PEMFCs). Besides the industrially well-established process for hydrogen generation by catalytic reforming of hydrocarbons, alternative processes have been proposed to foster the decarbonization of the energy sector, including thermochemical, electrolytic,[3,4] and photolytic ones such as alcohol reforming and autothermal reforming,[5] biomass gasification,[6] and photoelectrochemical (PEC) water splitting.[7] Nevertheless, carbon monoxide is generated as a byproduct and PEMFCs need the use of hydrogen containing less than 50 ppm CO to avoid poisoning of the Pt or Pt–Ru electrodes. CO preferential oxidation in hydrogen-rich stream (CO-PROX) is very promising because this simple and cost-effective reaction, usually performed in the 30–250 °C temperature range,[8] can be coupled to PEMFCs. In this configuration, hydrogen storage is not necessary, and it can be used for both automotive applications and stationary and portable power generation.[9]

The need to harvest and convert solar energy, an inexhaustible and clean source par excellence, has prompted intensive research efforts in this field, legitimizing the photocatalytic approach as one of the best options for sustainable future energy production.

Nowadays many semiconductors are investigated as photocatalysts, and among them, the most widely studied and applied is titanium dioxide, TiO_2. There are two well-known drawbacks of titania: its wide band gap, ranging from 3.0 eV of rutile to 3.2

Received: May 8, 2020
Accepted: July 20, 2020
Published: July 20, 2020

https://dx.doi.org/10.1021/acsami.0c08258
ACS Appl. Mater. Interfaces 2020, 12, 38019–38030

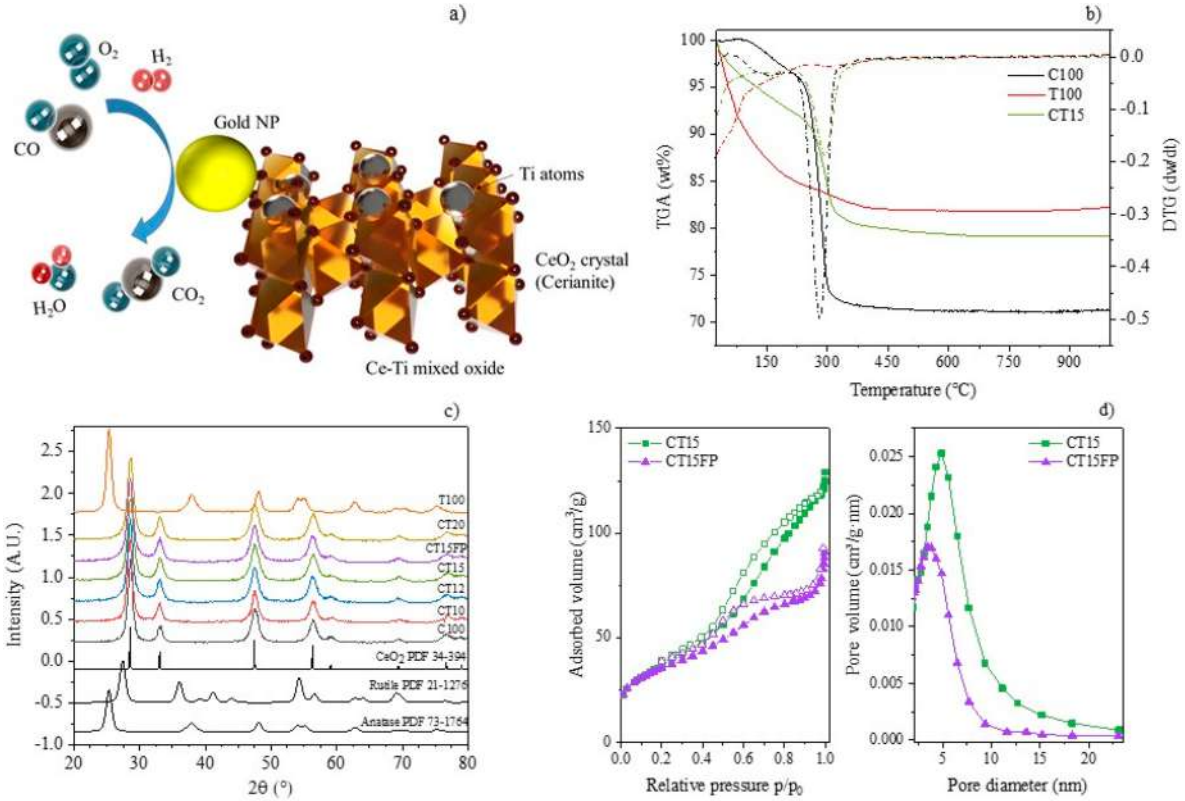

Figure 1. (a) Scheme of photo-CO-PROX in H_2-rich stream by applying Au NP decorated Ce−Ti mixed oxides. (b) TG/DTG of selected samples: C100, T100, and CT15 (solid lines for TG and dashed lines for DTG curves). (c) X-ray diffraction patterns of fresh CT*x* and T100 photocatalysts (JCPDS literature references of TiO_2 and CeO_2 polymorphs). (d) (left) N_2 adsorption−desorption isotherms at −196 °C of samples CT15 and CT15FP (both containing 15 wt % titania in ceria). Filled symbols refer to the adsorption branch, and empty symbols refer to the desorption one. (right) BJH pore size distributions of CT15 and CT15FP.

eV of anatase, which limits light absorption to the UV region, and the high recombination rate of electron−hole pairs.

A number of ways have been pursued to broaden the absorption range and to improve charge separation, such as metal and nonmetal doping, dye sensitization, and coupling with other semiconductors. A growing interest has recently emerged on photoenergy applications of ceria, CeO_2, and CeO_2-based catalysts.[10] The wide use of ceria as catalyst or a noninert support for catalysts has been associated in the literature with its unique ability to shuttle between Ce(III) and Ce(IV) states depending on whether it is present in an oxidizing or reducing atmosphere. Non-stoichiometric CeO_{2-x} compounds can be formed by reduction of Ce(IV) to Ce(III) with oxygen release and the concomitant formation of oxygen vacancies within the crystal structure, leading to a high oxygen mobility without suffering variations from its lattice, even after considerable loss of oxygen.[11] Thanks to this redox capability, known as oxygen storage capacity (OSC), cerium oxides are considered excellent oxygen buffers and are very active in oxidation reactions.[12] The theoretical band gap of CeO_2 is about 6.0 eV between the states of O 2p and Ce 5d;[13] nevertheless the experimental band gap is only around 3.2 eV, a value approaching that of other two semiconductors largely employed in photocatalysis, TiO_2 and ZnO.[14] Most probably this is due to the O 2p → Ce 4f transition, even though the origin of this reduced band gap is still controversial.[15]

Introduction of metal ions into the CeO_2 lattices can increase the density of oxygen vacancies and potentially improve the catalytic performance of CeO_2-supported metal catalysts, through changing the physical and chemical properties of the supports.[16,17] In particular, the preparation of CeO_2-based heterostructures have been investigated to reduce the band gap of pure CeO_2, by improving charge separation and/or hindering the recombination due to the novel structures and interfacial charge transfer, resulting in enhanced photocatalytic efficiencies.[18,19] The formation of CeO_2/TiO_2 composite photocatalysts has been reported, which showed catalytic activity superior to that of single CeO_2 and TiO_2.[20,21] Similarly, it has been proven that the morphology of CeO_2-based nanocomposites has a strong effect on the photoactivity of a catalyst.[22]

Highly active ceria-based catalysts can be designed by tuning the synthesis process to produce the desired morphologies and microstructures with controlled oxygen vacancies for the targeted reaction. Among others, a synthetic methodology to obtain flower-like ceria-based materials is available.[23−25] During the nucleation phase, under specific reaction conditions and in the absence of glycols or other soft surfactants, rare earths among them ceria can create a hierarchical structure composed of many microsheets, as petals forming a sort of flower.

Introducing metal nanocrystals on the semiconductors can offer unique capabilities to control the light−matter interaction of the support materials by harnessing the light absorption and decay properties of surface plasmon resonance (SPR).[26] As far as catalytic applications are concerned, the use of ceria requires in most cases combination with nanosized metal particles. Since the discovery of the exceptional catalytic properties of supported gold nanoparticles (Au NPs), Au nanoparticle catalysts have

https://dx.doi.org/10.1021/acsami.0c08258
ACS Appl. Mater. Interfaces 2020, 12, 38019−38030

Table 1. Textural Parameters, Gold Content and Band Gap Energy of Bare Supports and AuCT*x* Final Photocatalysts, as Well as Turnover Frequency (TOF) Values of CO Oxidation under Dark and Simulated Sunlight Irradiation for AuCT*x* Series

sample	Au[a] (wt %)	SA_{BET}[b] ($m^2\ g^{-1}$)	V_p[c] ($cm^3\ g^{-1}$)	crystallite size[d] (nm)	E_g[e] (eV)	TOF of CO oxidation[f] ($mmol \cdot g_{cat}^{-1} \cdot h^{-1}$) dark	light
C100	–	42	0.031	8.3 (CeO_2)	2.80	–	–
CT10	–	81	0.071	8.0 (CeO_2)	2.60	–	–
CT12	–	96	0.107	7.2 (CeO_2)	2.40	–	–
CT15	–	132	0.184	6.8 (CeO_2)	2.45	–	–
CT15FP	–	122	0.123	6.7 (CeO_2)	2.55	–	–
CT20	–	110	0.109	6.7 (CeO_2)	2.50	–	–
T100	–	52	0.041	14.8 (TiO_2)	3.10	–	–
AuC100	0.82	41	0.028	8.3 (CeO_2)	–	0.8	2.6
AuCT10	0.63	81	0.065	8.0 (CeO_2)	–	0.7	3.5
AuCT12	0.81	95	0.105	7.2 (CeO_2)	–	2.7	4.7
AuCT15	0.63	132	0.180	6.8 (CeO_2)	–	3.4	5.2
AuCT15FP	0.54	121	0.120	6.7 (CeO_2)	–	2.1	4.7
AuCT20	0.60	109	0.105	6.7 (CeO_2)	–	1.9	3.3
AuT100	0.69	50	0.040	14.7 (TiO_2)	–	1.5	3.6

[a]Determined by ICP-OES elemental analysis. [b]BET specific surface area determined by N_2 physisorption at −196 °C. [c]Specific pore volume calculated at $P/P_0 = 0.98$ by N_2 physisorption at −196 °C. [d]Crystallite size calculated by the Scherrer equation. [e]Band gap determined by diffuse reflectance (DR) UV−vis spectroscopy. [f]Gas hourly space velocity (GHSV) = 22 000 h^{-1}; $\lambda = 2$; 1.2% CO, 1.2% O_2, and 50.0% H_2 (vol %, He balance); T = 30 °C.

been the subject of numerous investigations for total and preferential CO oxidation.[27,28] Gold nanoparticles are the most prominent and investigated class in photocatalysis, since they present efficient absorption in the visible light region through localized surface plasmon resonance (LSPR)[29] and, supported on a semiconductor like titania, give rise to a Schottky barrier.[30] Collective oscillations of hot electrons close to the Au−support interface can occur upon visible light excitation. Hot electrons can overcome the Schottky barrier and be subsequently transferred to the conduction band of the adjacent semiconductor.[31] Furthermore, the presence of Au NPs can extend the lifetime of charge carriers that reach the surface of the semiconductor by enhancing the rates of electron−hole separation at their interface. Formation of highly energetic carriers is the most common mechanism exploited in SPR-mediated catalysis, although local heat generation and near-field enhancement are also prominent mechanisms in photocatalysis.[32]

The present work (see the scheme in Figure 1a) aims to investigate the photocatalytic behavior of Au NPs supported on CeO_2−TiO_2 (0−20 wt % TiO_2 loading) nanostructured matrixes in the CO preferential oxidation in H_2-rich stream (photo-CO-PROX), at room temperature and atmospheric pressure, under simulated solar light irradiation. The target application is H_2 purification in PEMFC technology.

The main concept behind this work is to modify the electronic band structure of ceria through the addition of titania, making it more suitable for interacting with free electrons excited in gold nanoparticles through SPR. The optical characterization demonstrates modulation of the optical band gap in the composite systems, accounting for the effectiveness of the proposed strategy.

Finally, we also assess how a controlled morphology can affect a multicomponent system, improving its photocatalytic performance.

EXPERIMENTAL SECTION

All details of the experimental activities are reported in the Supporting Information.

RESULTS AND DISCUSSION

Thermogravimetric (TG/DTG) analyses were performed on the CT*x* samples (C = ceria; T = titania; *x* = 0, 10, 12, 15, 20 wt % TiO_2) to determine the optimal calcination conditions required for the stepwise removal of organic residues and byproducts. The curves of C100, T100, and CT15 samples, taken as examples, are reported in Figure 1b. The thermogravimetric curves of the samples C100, CT10, CT12, CT15, and CT20, containing a titania loading between 0 and 20 wt %, exhibit a common trend. A first weight loss occurs, about 5−10 wt %, up to 200 °C, attributed to the decomposition and degradation of organic moieties derived from the synthesis (mainly titania precursor, titanium(IV) isopropoxide (TTIP)) and the desorption of physisorbed water.

Then, a second weight loss is recorded, about 25−30 wt %, in the range 280−350 °C, ascribed to the thermal decomposition of cerium hydrated carbonates and hydroxycarbonates formed during the synthesis by the reaction between cerium nitrate and potassium carbonate.[36] According to these data, the thermal treatment chosen for all the prepared samples was set at 450 °C.

Phase identification was performed by X-ray powder diffraction in the 2θ range 20−80° (Figure 1c). Pure ceria sample, C100, exhibits peaks emerging at 28.56, 33.08, 47.75, and 56.33° attributed to the cubic fluorite structure of cerium dioxide (database PDF 34-394); pure titania sample, T100, displays the characteristic peaks of anatase phase at 25.46, 37.92, 48.11, and 54.68° 2θ, in agreement with the values in the standard card (database PDF 73-1764), as expected by considering the calcination temperature used. Mixed oxide samples CT10, CT12, CT15, CT15FP (FP, fast precipitation), and CT20 exhibit the typical XRD profile of cerianite, with characteristic peaks indexed to the cubic fluorite structure. CeO_2 crystallite sizes, estimated from the full width at half-maximum of the 2θ = 28.5° diffraction peak of the CeO_2(111) face using

https://dx.doi.org/10.1021/acsami.0c08258
ACS Appl. Mater. Interfaces 2020, 12, 38019−38030

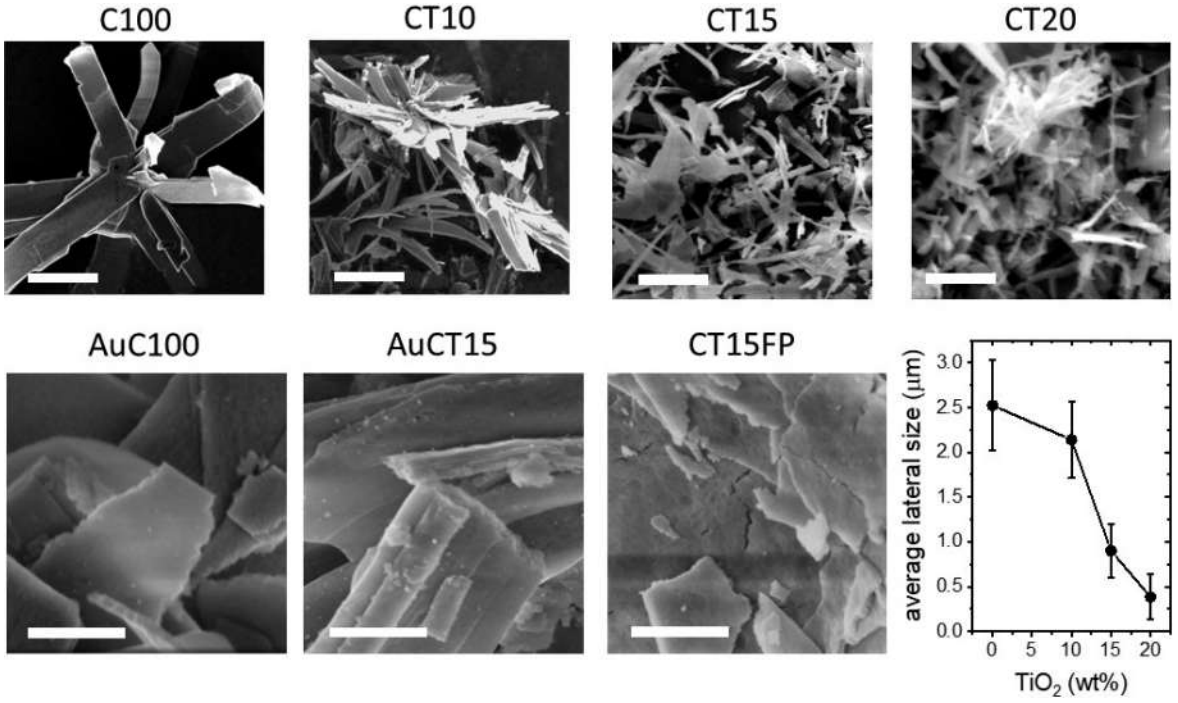

Figure 2. SEM images of the different samples after calcination, before and after Au sensitization. The markers correspond to 5 μm and 500 nm for the top and bottom rows, respectively. Bottom right panel: lateral size of the platelets as a function of TiO_2 content.

the Scherrer equation, are summarized in Table 1. Interestingly, all the Ce−Ti mixed oxides do not exhibit peaks related to the presence of titania polymorphs, even in the presence of a high TiO_2 loading (up to 20 wt %), and the crystalline structure of the composite materials is inferred as a CeO_2 cubic fluorite structure. Since the ionic radius of Ti^{4+} (0.68 Å) is much smaller than that of Ce^{4+} (1.01 Å) and the content of cerium is much higher than that of titanium, it can be suggested that Ti^{4+} ions could incorporate into the lattice of CeO_2 to replace Ce^{4+} ions, leading to the formation of Ce−Ti solid solution, $Ce_{1-x}Ti_xO_2$.[37] This is corroborated by the decrease in CeO_2 crystallite size by increasing the TiO_2 loading, passing from 8.3 nm for C100 sample to 6.7 nm for CT20 sample, and by a slight shift toward higher angles of the main reflection peaks of cerium dioxide, suggesting a slight distortion of the ceria lattice due to the incorporation of titanium(IV) ions.

XRD was also carried out after deposition−precipitation of gold nanoparticles on the final AuCT*x* catalysts (not shown): no modification of the titania−ceria phases was detected, nor were gold-containing phases discerned in the XRD patterns, most probably due to the low Au concentration (0.54−0.82 wt %), below the XRD detection limit.

The porous nature of the synthesized materials, prepared by a controlled and very slow addition of an alkaline solution to a Ti and Ce precursor solution, followed by a long crystallization step, was evaluated by N_2 physisorption at −196 °C, and the textural properties are reported in Table 1. The isotherms of the CT*x* series belong to the type IV profile, according to the IUPAC classification,[38] with a small hysteresis loop suggesting that the very slow coprecipitation led to the formation of mesoporous solids, with a mesoporosity also originated by interparticle voids. Pore size distribution is narrow and centered between 3.5 and 7 nm, which is very interesting, considering that the synthesis was carried out in the absence of any kind of surfactants. In Figure 1d, isotherms and Barrett−Joyner−Halenda (BJH) pore size distributions of samples CT15 and CT15FP, taken as an example, are reported.

Pure ceria, C100, displays a specific surface area of 42 $m^2\ g^{-1}$ and pure titania, T100, has a specific surface area of 52 $m^2\ g^{-1}$. The addition of titania to the ceria matrix increases the support surface area by more than double, which is considered to possibly contribute to a higher catalytic activity and can be due to incorporation of Ti into the ceria lattice, with the formation of a solid solution.[39] The change in the Brunauer−Emmett−Teller (BET) surface area due to the addition of Au NPs can be considered as negligible for all the samples (Table 1) and is most probably due to a very slight pore blocking of the support by gold nanoparticles.

The surface morphology of the samples, before and after calcination, was investigated by SEM microscopy. No morphological changes were detected after calcination. The materials are characterized by the presence of extended and thin 2D sheets (Figure 2).

The addition of titania drastically reduces the lateral dimensions of the platelets, compared to the C100 sample (see the measured lateral size from SEM in Figure 2). A general view revealed that all the calcined samples of CT*x* series are made up by microneedles.

For comparison purposes, the sample CT15FP was synthesized by a traditional coprecipitation method, with a faster basification and a consequent lower nucleation time. SEM analysis of this sample revealed a more compact morphology, compared to the CT*x* series, even if the most peculiar differences were highlighted only through HR-TEM and were not visible through SEM analysis. As expected, pure titania sample, T100, prepared by use of the same synthetic procedure used for the ceria-containing samples, did not exhibit any organized morphology (Figure S1).

EDS elemental analysis of the CT*x* series confirmed the presence of titanium in the supports, in a concentration

https://dx.doi.org/10.1021/acsami.0c08258
ACS Appl. Mater. Interfaces 2020, 12, 38019−38030

approaching the nominal amount (even though the presence of TiO_2 did not modify the XRD pattern). For the sake of an example, the EDS analysis of CT15 and CT15 FP samples has been reported (Figure S2): compared to the nominal Ti/Ce ratio (w/w) (0.13, corresponding to 15 wt % TiO_2), the composition measured by EDS is slightly higher (0.14) for CT15 support and lower (0.10) for CT15FP sample, most probably due to the different synthetic methodologies employed.

TEM characterization was carried out on some representative samples to have an insight into the nanostructure composition of the Ce−Ti composite oxide and the nanoscale arrangement of Au nanoparticles.

Figure 3 displays the results of elemental maps extracted from STEM−EDX analysis of AuCT15 and AuCT20, in addition to

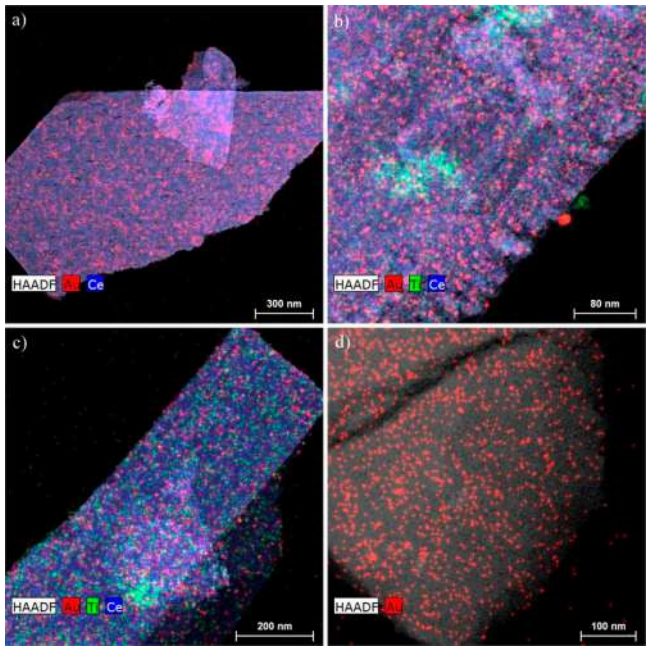

Figure 3. STEM images with EDX maps superimposed of samples (a) AuC100, (b) AuCT15, (c) AuCT20, and (d) AuT100.

AuC100 and AuT100 as reference samples where Au nanoparticles are supported on either pure Ce- or Ti-based oxide. For all samples, Au-related signal is distributed on the whole supporting material, with no evidence of aggregation or segregation into large-scale nanoparticles.

No difference is observed among the samples in terms of Au distribution, pointing out that Au NPs decoration is independent of the metal oxide composition and shape.

As expected, no specific heterostructure is observed in the mixed oxide samples, where Ti content is distributed quite randomly on the Ce oxide supporting material, even though some small titanium-rich clusters are also present.

Figures 4 and 5 report the HR-TEM analysis of AuCT15 and AuCTFP15 samples, chosen as representative samples due to the large surface area and the optimal photocatalytic properties (AuCT15) and as a benchmarking standard (AuCT15FP), as discussed later. AuCT15 sample is characterized by a hierarchical structure composed by compact needlelike microstructures, as previously observed by SEM, fully decorated by 2−10 nm large nanoparticles with similar densities and crystal structures. In contrast, samples with lower and higher Ti content do not display this complex heterostructure (Figure S3).

Both the needlelike structure and the nanoparticles covering them display a highly crystalline lattice, whose pattern is compatible with the cubic fluorite CeO_2 structure, also known as cerianite, consistent with XRD analysis results.

SAED analysis on the composite highlights the polycrystalline nature of the material, as well as the perfect matching to the cerianite phase (Figure S4). No evidence of AuNPs is directly observed on the HR-TEM micrograph due to the superposition of the crystalline nanoparticles and the large thickness of the nanoneedles.

However, STEM-HAADF micrographs (Figure 4c) highlight the presence of denser, high-atomic-weight nanoparticles, whose contrast is compatible with pure Au. Both large (>15 nm) Au NPs and smaller (<10 nm) Au NPs can be noticed, highlighted with green and red arrows, respectively. The composition of these nanoparticles is further confirmed by EDX mapping on the same area. This technique also displays the presence of both Ce and Ti on the large needlelike microcrystals, as well as the decorating nanoparticles. By comparing the relative contents of Ti and Ce on the two different nanostructures, we can observe how the ratio Ti/Ce shifts from 0.14 in the needles, fully fitting with the expected content, to 0.41 in the decorating nanoparticles. Thus, we infer that the Ti-rich CeO_2 nanoparticles are resulting from the segregation of excess Ti in the reaction environment, whose slightly different atomic radius, with respect to Ce, might induce strain in the growing crystallite and limit the size to a few nanometers.

For the sake of comparison, AuCT15FP sample (Figure 5) was also analyzed. The fast-precipitated ceria-based microstructures are strongly different from the slow-precipitated sample, with a layered structure forming large platelets, as previously observed by SEM analysis. No evidence of the randomly dispersed Ce/Ti-based nanoparticles is observed. The ceria platelets are clean and display a porous surface in some areas. The HR-TEM micrograph displays the same pattern that was observed in the slow-precipitation process sample, compatible with cerianite phase, as displayed by the fast Fourier transform (FFT) in the insets (Figure 5). The surface of the sample was clearly irregular and porous, but the size of the crystal was this time exceeding the typical size of the high-magnification image, suggesting a larger domain size. The Au nanoparticles can be clearly recognized on the surface of the layered microcrystal in both HR-TEM and STEM micrographs, but no evidence of small (<10 nm) Au NPs is observed, as confirmed by EDS mapping. Due to the lower thickness of the supporting CeO_2 material, the typical diffraction fringes of cubic Au (2.3 Å) can be observed on the FFT of the HR-TEM micrograph.

Au-based samples were analyzed by X-ray photoelectron spectroscopy (XPS), to obtain information on the surface composition and the oxidation states of gold, titanium, and cerium on the surface. Figure 6 compiles the corresponding core level signals, and Table 2 lists the surface atomic composition and the Au 4*f* binding energy (BE) values of Au species.

The titanium signal (Figure 6) presented a doublet, whose Ti $2p_{3/2}$ component is centered at 458.5 eV in AuT100 sample. The BE value is typical of Ti^{4+} species in TiO_2 structure.[40] The signal is slightly shifted to higher binding energy values when the titania content is higher.

On the other hand, Ce 3*d* core level spectra showed, in all cases, four spin−orbit doublets denoted as $\nu(n)$ and u(n): three

https://dx.doi.org/10.1021/acsami.0c08258
ACS Appl. Mater. Interfaces 2020, 12, 38019−38030

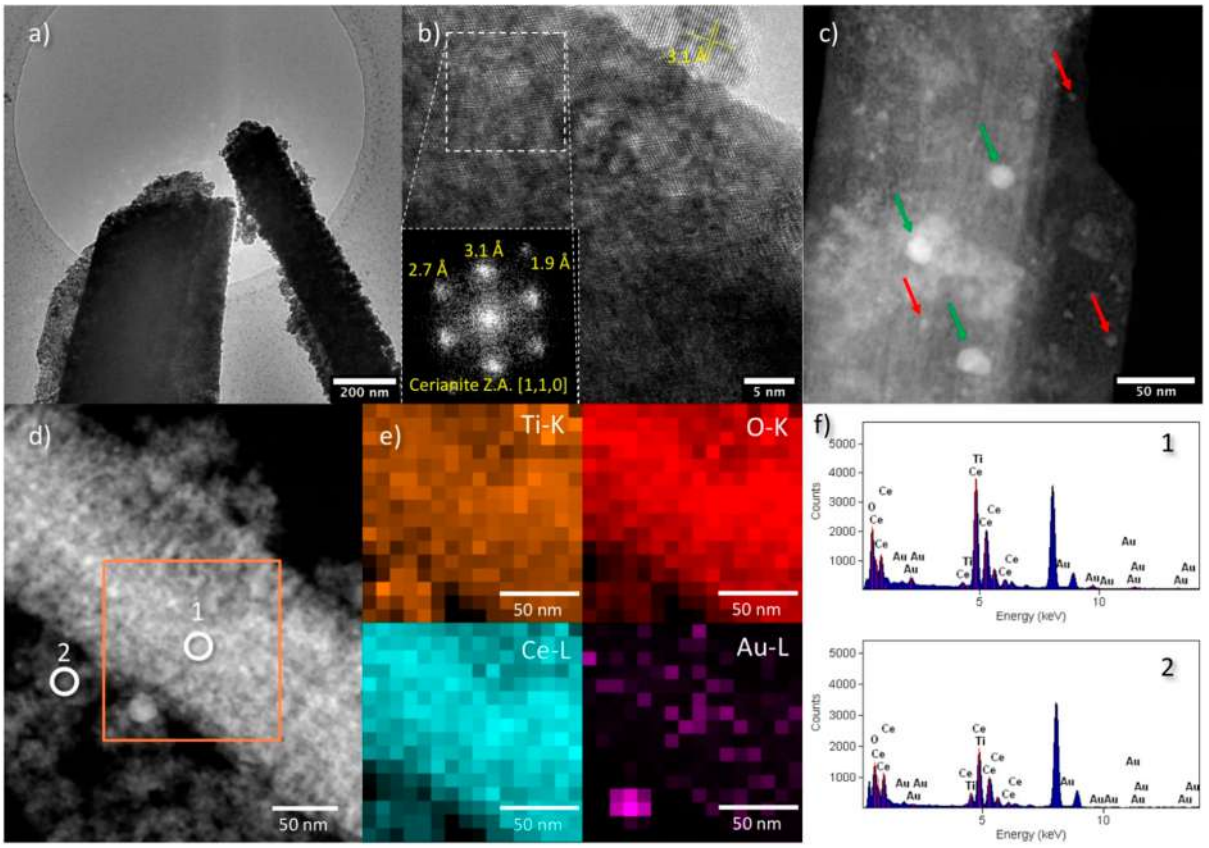

Figure 4. HR-TEM characterization of AuCT15 sample. (a) Low-magnification and (b) high-magnification HR-TEM micrographs, with FFT in the inset. (c, d) STEM-HAADF images of the composite nanomaterial and (e) relative EDX mapping for Ti, O, Ce, and Au. (f) EDX spectra acquired in the corresponding spot highlighted in (d).

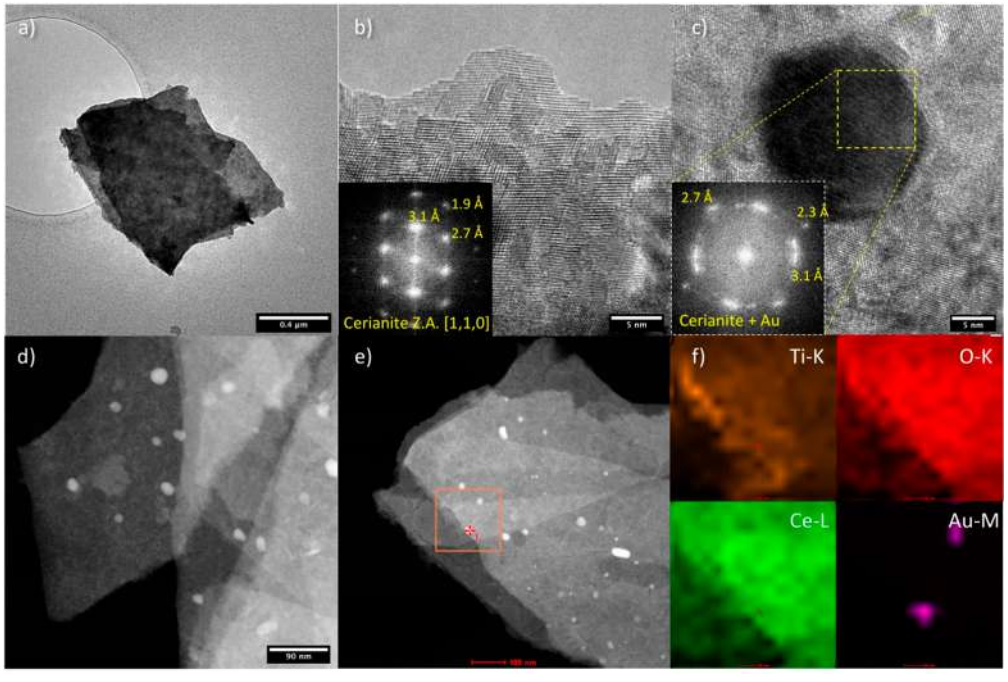

Figure 5. HR-TEM characterization of AuCTFP15 sample. Specifically, (a) low-magnification and (b, c) high-magnification HR-TEM micrographs, with FFT in the insets. (d, e) STEM-HAADF images of the composite nanomaterial and (f) relative EDX mapping for Ti, O, Ce, and Au.

ascribed to the presence of Ce^{4+} (ν (~882.2 eV) and u (~900.7 eV); ν'' (~888.8 eV) and u″ (~907.2 eV); ν''' (~898.2 eV), u‴ (~916.5 eV)) and one due to Ce^{3+} species (ν' (~884.5) and u′ (~903.3 eV)).[41] It is clearly observed that Ce^{4+} is the main oxidation state of cerium in these samples. The presence of Ce^{3+} species is only evidenced by the contribution at 884.5 eV (ν'),

https://dx.doi.org/10.1021/acsami.0c08258
ACS Appl. Mater. Interfaces 2020, 12, 38019−38030

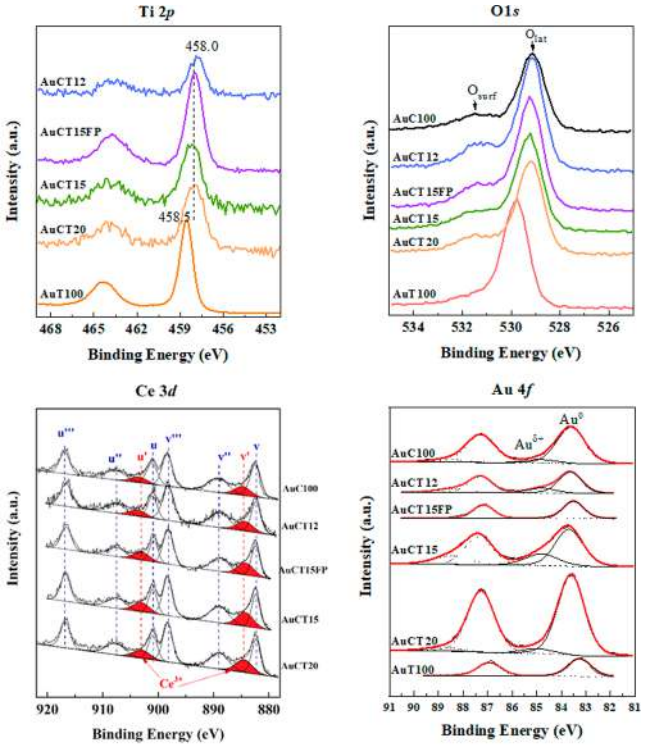

Figure 6. Ti 2*p*, O 1*s*, Ce 3*d*, and Au 4*f* XPS signals of the photocatalysts.

being a shoulder of the signal at 882.2 eV (ν). The decomposition of Ce 3d core level spectra (Figure 6) showed as described above eight peaks corresponding to four spin−orbit components (the spin−orbit splitting was about 18.6 eV). The ratio Ce $3d_{5/2}$/Ce $3d_{3/2}$ was fixed at 1.5 considering the study of Bêche et al.[42] It was possible to quantify the surface Ce^{4+}/Ce^{3+} ratio present for each sample (Table 2). It is evidenced that titania incorporation improves ceria reducibility by following the order AuCT15 ≈ AuCT15FP > AuCT20 > AuCT12 > AuC100. It is interesting to notice that the preparation method does not alter ceria reducibility, presenting AuCT15 and AuCT15FP samples with similar Ce^{4+}/Ce^{3+} values. Moreover, if the signal at ca. 882 eV is considered, a slight shift to lower BE is noticed by incorporating Ti into the ceria network. The observed shift in Ce and Ti signals suggests an interaction between both components. Sheerin et al.[43] prepared mixed Ce−Ti oxides containing different Ce and Ti loadings, and a similar shift in Ti signal was observed. XRD and textural properties also pointed in this direction, to the formation of a Ti−Ce solid solution.

Considering the O 1s signal, Ce-containing samples presented two contributions: one at 529.1−529.4 eV, associated with lattice oxygen in ceria (O_{lat}), and another one at 531.3−531.7 eV, due to the presence of surface oxygen (O_{surf}),[44] due to the presence of defect sites within the oxide crystal, adsorbed oxygen, or hydroxide species on the surface of the samples. If the spectra are compared, by increasing the titania loading, the main signal hardly changes, being closer to the BE related to CeO_2 (529.1 eV) than to that of TiO_2 (529.9 eV). Instead, AuT100 compound possesses the main signal located at 529.9 eV, typical of TiO_2 species.[45] Considering the surface oxygen signal, it is reported that the area and intensity of this signal provide an indication of oxygen vacancies in the host lattice.[46] The spectra were decomposed (not shown), and the quantification of this contribution has been included in Table 2 as the O_{surf}/O_{lat} ratio. As observed, AuCT*x* samples present a greater amount of surface oxygen species than pure ceria and titania ones. Nonetheless, the preparation method does not influence this ratio if data related to AuCT15 and AuCT15FP samples are compared.

Finally, the Au 4*f* signal presented the most intense Au $4f_{7/2}$ and Au $4f_{5/2}$ binding energy peaks at ∼83.4−87.3 eV, corresponding to Au^0.[47] A less intense contribution located at ∼85.0 and 88.6 eV was also observed and assigned to partially reduced surface gold species, $Au^{\delta+}$.[48,49] On the basis of this, it can be stated that gold exists mainly in a metallic state, but there is a proportion of $Au^{\delta+}$ on the surface. The support composition does not alter the Au 4*f* BE value but does alter the percentage of each species, as observed in Table 2.

The surface atomic composition indicated that, although there is not a clear trend between the Au/(Ce + Ti) ratio and the support composition, AuCT20 sample presented the highest Au/(Ce + Ti) ratio, therefore indicating a greater Au surface exposure. The AuCT15 sample, instead, presents the highest amount of $Au^{\delta+}$ species on the surface. The literature reported that the presence of these partially reduced gold species is highly beneficial for the catalytic activity in the CO oxidation reaction. Escamilla-Perea et al.[49] studied the CO oxidation on SBA-15-supported gold nanoparticles decorated by CeO_2. These authors explained the CO oxidation by considering the collaborative effects of the high surface exposure of $Au^{\delta+}$ and Ce^{3+} species, derived from XPS and the IR band assigned to CO on $Au^{\delta+}$. A similar dependence was reported previously by Minicò et al.[50] Moreover, we[51] also observed that the presence of Ce^{3+} on the catalyst surface improved the activity of zirconia-supported $CuO-CeO_2$ catalysts in the carbon monoxide oxidation reaction. Therefore, the presence of $Au^{\delta+}$ species and Ce^{3+} ions on the surface seems to improve the catalytic activity of these systems.

The photoresponsive behavior of the samples was explored by DRUV−vis spectroscopy to determine the energy gap value of the supports (Figure 7 and Table 1), estimated from the linear extrapolation of $(\alpha h\nu)^{1/2}$ versus photon energy.

Titania sample, T100, shows an E_g value of 3.10 eV, typical of pure titania, slightly lower than that of anatase polymorph. Pure ceria, C100, displays a much lower band gap value (2.79 eV)

Table 2. Atomic Ratios and Au 4f Binding Energy Values for the AuCT*x* Photocatalysts

sample	Au^0 (eV)	Au^0 (%)	$Au^{\delta+}$ (eV)	$Au^{\delta+}$ (%)	Ce^{4+}/Ce^{3+}	Au/(Ce + Ti)	$Au^{\delta+}$/(Ce + Ti)	O_{surf}/O_{lat}
AuC100	83.6	89.2	84.9	10.8	6.9	0.024	0.26	0.31
AuCT12	83.6	77.7	84.8	22.3	5.9	0.016	0.36	0.37
AuCT15	83.7	71.2	84.8	28.8	4.3	0.021	0.61	0.37
AuCT15FP	83.5	100	–	–	4.4	0.011	0	0.34
AuCT20	83.6	93.0	85.0	7.0	5.2	0.041	0.29	0.32
AuT100	83.3	100	–	–	–	0.014	0	0.15

https://dx.doi.org/10.1021/acsami.0c08258
ACS Appl. Mater. Interfaces 2020, 12, 38019−38030

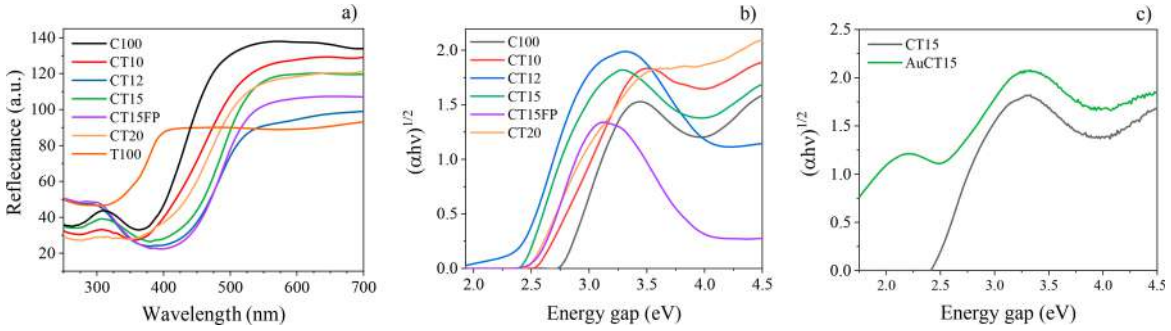

Figure 7. Optical properties of the CT*x* series before Au sensitization. (a) Absorption spectra. (b) Tauc analysis: $(\alpha h\nu)^{1/2}$ vs photon energy curves. (c) $(\alpha h\nu)^{1/2}$ vs photon energy curves of the ceria−titania photocatalyst before (CT15) and after (AuCT15) gold sensitization.

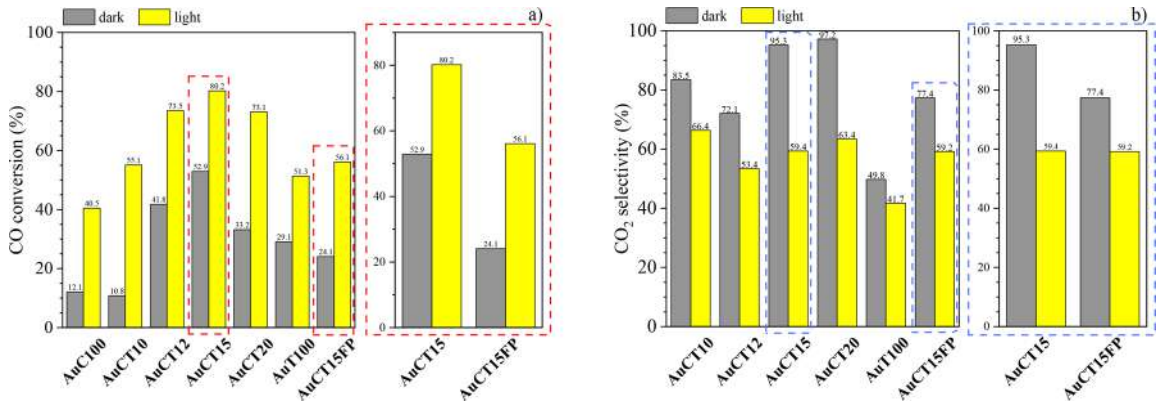

Figure 8. (a) CO conversion and (b) CO_2 selectivity values (%), for CO preferential oxidation in excess of hydrogen in dark and simulated solar light modes. Operating conditions: T = 30 °C; GHSV = 22 000 h^{-1}; feed gas, 1.2% CO, 1.2% O_2, and 50.0% H_2 (vol %, He balance). In the right part of each image, the comparison is reported between the samples AuCT15 and AuCT15FP.

with respect to that usually reported in the literature for bulk CeO_2, with a red shift attributed to the presence of Ce^{3+} at the grain boundaries, which forms some localized gap states in the band gap.[52]

As for ceria−titania mixed oxides, it has been reported[53] that the migration of Ti^{4+} ions into the ceria lattice at the oxide−oxide interface of CeO_2−TiO_2 favors the formation of Ce^{3+} sites, which can be very useful in catalytic processes. For example, the presence of Ce^{3+} ions in M/CeO_x/TiO_2 (M = Au, Cu, Pt) systems seems to favor the water dissociation, making these systems excellent catalysts for the H_2 production through the water gas shift reaction.[54,55] Moreover, in ceria−titania mixed oxides, the Ce^{3+} species seem to introduce additional states in the band gap, corresponding to the partially occupied 4f levels, and thereby reduce the band gap up to 2.2 eV.[56]

All the prepared CT*x* systems show energy gap values lower than those of pure oxides, ranging between 2.34 and 2.57 eV (Figure 7b), with a red shift that could be ascribed to the presence of additional localized energy levels (oxygen vacancies) within the band gap, absorbing relatively low energy photons.

In Figure 7c the Tauc plots of the sample with 15 wt % TiO_2 loading, before and after Au sensitization, are reported. The observed LSPR broad band centered at ca. 2.20 eV (absorption at about 560 nm) can be attributed to the presence of Au NPs deposited on the supports by deposition−precipitation method. The low intensity in signal could be ascribed to the very low amount of gold (0.54−0.82 wt %), as confirmed by ICP-OES analysis (Table 1).

The AuCT*x* catalysts were finally tested in the CO preferential oxidation in excess of hydrogen at room temperature and atmospheric pressure under dark and simulated solar light irradiation, and their performances are shown in Figure 8. TOF values (mmol·g_{cat}^{-1}·h^{-1}) of CO oxidation are reported in Table 1.

The photocatalytic behavior of the bare supports, both pure and mixed oxides, was investigated, and the response was found negligible (few percentage units, not shown) both in dark mode and under solar light irradiation. Gold-based samples, on the contrary, showed a very interesting catalytic behavior, both in dark conditions and under sunlight irradiation. On the other hand, since the discovery of the exceptional catalytic properties of nanosized supported gold particles, it is well-known that Au catalysts are active in the total and preferential CO oxidation reactions.[27,28]

As shown in Figure 8, the CO conversion versus TiO_2 content plot of AuCT*x* samples shows a trend depending on the increasing amount of TiO_2, which seems to have a significant effect on the catalytic activity, improving the conversion passing from 0 wt % TiO_2 loading (AuC100) up to 15 wt % TiO_2 loading (AuCT15). Conversely, an excessive amount of titania (AuCT20 sample) not only does not further improve the catalytic activity but also diminishes the CO conversion.

AuCT15 is, by far, the most active sample, with a CO conversion of 52.9% in dark mode and 80.2% under sunlight, respectively, as also highlighted by the TOF values of CO oxidation (Table 1). This catalyst also exhibits a much higher activity in comparison with both pure oxide systems, AuC100 and AuT100. In detail, the CO conversion values in dark mode are 12.1, 29.1, and 52.9% for AuC100, AuT100, and AuCT15, respectively. Under simulated solar light irradiation, the CO

https://dx.doi.org/10.1021/acsami.0c08258
ACS Appl. Mater. Interfaces 2020, 12, 38019−38030

Table 3. Catalysts Used in Photo-PROX Reaction in Recent Years

catalyst	Au (wt %)	reaction temp (°C)	irradiation source	CO conversion (%)	CO_2 selectivity (%)	ref
Au/TiO_2	1.0	25	visible light	25	60	65
Au/TiO_2@CuO	1.0	25	visible light	70	85	65
Au/TiO_2 nanorods	1.0	30	solar light	40	100	33
Au/TiO_2-PANI	1.0	25	visible light	55	80	66
Au/meso-TiO_2	0.47	30	solar light	95	69	67
AuCu/SBATi	1.5	30	solar light	80	80	68
AuCT15	0.63	30	solar light	80	60	this work

conversion values are 40.5, 51.3, and 80.2% for AuC100, AuT100, and AuCT15, respectively.

Cerium oxide has been proven as an excellent catalyst support to be used in in the CO-PROX reaction, and mechanistic studies have shown that the lattice oxygen plays a crucial role, since the reaction follows a Mars−van Krevelen mechanism,[57,58] according to which CO is chemisorbed on Au NPs[59] and oxygen is supplied by the support, generating reduced Ce^{3+} species that are oxidized back with oxygen from the feed.

The incorporation of a second metal into the CeO_2 lattice, as TiO_2, seems to enhance ceria reducibility, participating in the Mars−van Krevelen mechanism and eventually improving the catalytic performance both in the dark and under sunlight irradiation. This could explain the better performance of AuCT15 sample with respect to AuC100 and AuT100. Moreover, as emerged from XPS analyses (Table 2), the incorporation of titania into the CeO_2 lattice improved the reducibility of ceria by increasing the amount of Ce^{3+} species and altered the Au oxidation state on the surface favoring the presence of partially reduced gold. The most active sample, AuCT15, displays not only the highest percentage of Ce^{3+}, but also by far the largest amount of partially reduced Au species on the surface, indicating that those species might be directly involved in the reaction mechanism. Further addition of TiO_2 up to 20 wt % in CeO_2 (AuCT20) gave rise to a decrease in the textural properties (i.e., specific surface area), in Ce^{3+} and $Au^{\delta+}$ amounts on the surface, and eventually in the CO conversion, in both dark and simulated solar light modes.

Along with the CO conversion efficiency, selectivity toward CO_2 was also investigated, and the results are reported in Figure 8b. Selectivity values in the CO-PROX are the result of the simultaneous CO and H_2 oxidation reactions, both occurring in the presence of molecular oxygen catalyzed by metal oxides. The desired reaction is clearly the CO oxidation, whereas H_2 oxidation is highly undesirable due to H_2 consumption (needed to feed a PEMFC). Nevertheless, as 100% of selectivity is usually not attainable, H_2 oxidation usually takes place and H_2O forms, reducing the activity and selectivity of the catalyst. It should be noted that, considering the reaction stoichiometry, the oxygen excess factor used (λ),[34,35] and the CO conversion values, the O_2 consumption is attributable to both oxidation reactions. Nevertheless, under both modes all the catalysts exhibit higher selectivities for CO oxidation compared to the undesired H_2 oxidation, as is typical in Au-based systems.[60,61] However, the observed CO_2 selectivity values are lower under simulated light irradiation. This is probably due to the simultaneous increase of the hydrogen oxidation due to the light irradiation, even though the factors governing photocatalytic activity in the CO-PROX reaction are not yet fully understood.

A durability test was performed on AuCT15 sample, and the CO conversion trend is reported in Figure S5. The reaction was monitored for 24 h, using GHSV = 22 000 h^{-1}; λ = 2; and 1.2% CO, 1.2% O_2, 50% H_2, and He balance (vol %). After switching on of the simulated solar light, the catalyst showed a diminution of CO conversion from 82 to 78% within the first 6 h, remaining nearly stable (74.4%) for the further operation time and suggesting a very good physicochemical stability of this multicomponent system.

Considering the reaction carried out in dark mode operating conditions, the "traditional" CO-PROX, and comparing the results obtained for the AuCT15 sample with the literature data, a maximum of 85% CO conversion at 100 °C with a selectivity to CO_2 of about 50% was obtained by Rossignol et al.[62] with 1.47 wt % Au/TiO_2 catalyst. Avgouropoulos et al.[63] reached 96% CO conversion with 3% Au/CeO_2 at 90 °C with a selectivity of 39%. A maximum CO conversion of 96% at 135 °C was reached by Ivanova et al.[64] on 1.95% Au/CeO_2. Considering the very low temperature at which the catalytic reaction has been performed in this study, 30 °C, and the very low Au loading, 0.63 wt %, we can conclude that the sample AuCT15 exhibits an outstanding activity in selectively oxidizing CO in dark conditions. Some examples of photocatalysts used for the so-called photo-PROX are listed in Table 3. Considering that most of the reference catalysts show a much higher Au loading and/or have been tested under visible light irradiation[65,66] (a solar light source is by far less energetic), it can be concluded that the sample AuCT15 displays a very good catalytic performance also in the photo-PROX reaction if compared to the literature data.

A comparison was finally made between the samples containing about 15 wt % titania and prepared by two different coprecipitation methods: a slow basification for the AuCT15 sample and a much faster coprecipitation for the AuCT15FP system, leading to very different morphological and catalytic properties. In fact, as evidenced by SEM and HR-TEM analysis, AuCT15 showed a hierarchical structure formed by compact needle-like microstructures decorated by Ti-rich nanoparticles. On the contrary, AuCT15FP did not show any self-organized structure, presenting a layered structure formed by large platelets, with no evidence of the randomly dispersed Ce/Ti-based nanoparticles.

By comparing the CO conversion values of these two catalysts (Figure 8a), the one prepared by a slow coprecipitation method displays a much higher catalytic activity both in dark conditions and under simulated sunlight irradiation. The CO conversion value is 52.9% for the sample AuCT15 and less than half, 24.1%, for AuCT15FP, with a gap of 28.8%. Under solar light irradiation, the CO conversion values are 80.2% for AuCT15 and 56.1% for AuCT15FP, with a difference of 24.1%.

The highest catalytic performance exhibited by the sample AuCT15 could be attributed to several factors, including the high specific surface area and total pore volume, the higher concentration of Ce^{3+} species, and the lower size of Au NPs.

Finally, the synergistic effect of gold NPs deposited on the highly porous ceria−titania network has to be taken into

https://dx.doi.org/10.1021/acsami.0c08258
ACS Appl. Mater. Interfaces 2020, 12, 38019−38030

account. The very finely dispersed gold nanoparticles, not detectable in our XRD patterns, appear to be very active in this photoreaction, in part due to the stabilization by the ceria support of partially reduced Au species, $Au^{\delta+}$, as detected by XPS measurements, highly active for the CO oxidation reaction and in part related to the enhancement of the light absorption, thanks to the larger bandwidth caused by the LSPR phenomenon.

CONCLUSIONS

In summary, we investigated the catalytic properties toward the photo-CO-PROX reaction of CeO_2−TiO_2 mixed oxides obtained through a slow and surfactant-free coprecipitation method and decorated by Au nanoparticles deposited by deposition−precipitation. The variation of the TiO_2 content in the mixed oxide results in significant textural and morphological changes of the supports, which display a specific surface area ranging between 81 and 132 $m^2\ g^{-1}$ and are mainly composed of micrometer sized thin platelets. The dimension of the platelets decreases with the increase of TiO_2 content. For a specific composition (15 wt %) a hierarchical structure is formed, in which the platelets are conformal decorated by small, Ti-rich oxide nanoparticles. Au nanoparticles are finely and homogeneously dispersed at the surface of the oxides and present a quite broad size distribution.

It is evidenced that the reducibility of ceria and gold oxidation state is altered by the incorporation of Ti into the ceria lattice. In this regard, the amount of Ce^{3+} and partially reduced gold $Au^{\delta+}$ species is improved in the CT*x* samples in comparison with pure oxides, with the AuCT15 sample displaying, not only the highest percentage of Ce^{3+}, but also the largest amount of partially reduced Au species on the surface and reported as catalytically active in the CO oxidation reaction.

The mixed oxides present an optical energy gap far below the theoretical one for pure ceria and titania, enabling direct exploitation of solar light for photocatalysis. The presence of Au NPs further broadens the absorbance to lower energy photons, close to the yellow region of the solar spectrum, thanks to LSPR.

We tested the compounds toward the preferential photo-oxidation of CO to CO_2 in excess of H_2 under simulated solar light irradiation at room temperature and atmospheric pressure, resulting much more active than a sample with a nonorganized structure prepared, as a benchmark, by a fast coprecipitation method. The most efficient sample exhibits CO conversions of 52.9 and 80.2% and CO_2 selectivities equal to 95.3 and 59.4% in dark and simulated solar light modes, respectively. We found a clear morphology−functionality correlation in our systematic analysis, with CO conversion maximized for a TiO_2 content equal to 15 wt %.

These results represent a promising step toward the preparation of an effective system for CO preferential oxidation in H_2-rich stream. The synthetic route is environmentally friendly and low cost, providing a potential solution for the open issue of H_2 stream purification in PEMFCs.

ASSOCIATED CONTENT

Supporting Information

The Supporting Information is available free of charge at https://pubs.acs.org/doi/10.1021/acsami.0c08258.

Syntheses of CeO_2−TiO_2 mixed oxides and Au-NPs/CeO_2−TiO_2 photocatalysts; characterization of catalysts; test of catalytic activity; SEM, TEM, EDS; SAED, time on stream test (PDF)

AUTHOR INFORMATION

Corresponding Authors

Alberto Vomiero − *Department of Molecular Sciences and Nanosystems, Ca' Foscari University of Venice, 30172 Mestre Venezia, Italy; Division of Materials Science, Department of Engineering Sciences and Mathematics, Luleå University of Technology, 97187 Luleå, Sweden;* orcid.org/0000-0003-2935-1165; Email: alberto.vomiero@unive.it, alberto.vomiero@ltu.se

Elisa Moretti − *Department of Molecular Sciences and Nanosystems, Ca' Foscari University of Venice, 30172 Mestre Venezia, Italy*; Email: elisa.moretti@unive.it

Authors

Antonia Infantes-Molina − *Departamento de Química Inorgánica, Cristalografía y Mineralogía (Unidad Asociada al ICP-CSIC), Facultad de Ciencias, Universidad de Málaga, 29071 Málaga, Spain;* orcid.org/0000-0001-6360-773X

Andrea Villanova − *Department of Molecular Sciences and Nanosystems, Ca' Foscari University of Venice, 30172 Mestre Venezia, Italy*

Aldo Talon − *Department of Molecular Sciences and Nanosystems, Ca' Foscari University of Venice, 30172 Mestre Venezia, Italy*

Mojtaba Gilzad Kohan − *Division of Materials Science, Department of Engineering Sciences and Mathematics, Luleå University of Technology, 97187 Luleå, Sweden*

Alessandro Gradone − *CNR-IMM Bologna Section, 40129 Bologna, Italy; Chemistry Department "Giacomo Ciamician", University of Bologna, 40126 Bologna, Italy*

Raffaello Mazzaro − *CNR-IMM Bologna Section, 40129 Bologna, Italy;* orcid.org/0000-0003-4598-9556

Vittorio Morandi − *CNR-IMM Bologna Section, 40129 Bologna, Italy;* orcid.org/0000-0002-8533-1540

Complete contact information is available at: https://pubs.acs.org/10.1021/acsami.0c08258

Notes

The authors declare no competing financial interest.

ACKNOWLEDGMENTS

A.I.-M. thanks the Ministry of Science, Innovation and Universities of Spain (RTI2018-099668-B-C22 and RyC-2015-17870) and Junta de Andalucía of Spain (UMA18-FEDERJA-126). A.I.-M. also thanks the Ministry of Science, Innovation and Universities of Spain for a Ramón y Cajal contract (RyC-2015-17870). A.V. and M.G.K. acknowledge the Kempe Foundation, the Knut & Alice Wallenberg Foundation, and the LTU Lab fund program for partial support. A.G., R.M., and V.M. acknowledge the European Union's Horizon 2020 research and innovation program under GrapheneCore2 785219—Graphene Flagship for partial funding.

REFERENCES

(1) Eftekhari, A. Electrocatalysts for Hydrogen Evolution Reaction. *Int. J. Hydrogen Energy* **2017**, *42*, 11053−11077.

(2) Carrette, L.; Friedrich, K. A.; Stimming, U. Fuel Cells-Fundamentals and Applications. *Fuel Cells* **2001**, *1*, 5−39.

(3) Han, W.; Zang, C.; Huang, Z.; Zhang, H.; Ren, L.; Qi, X.; Zhong, J. Enhanced Photocatalytic Activities of Three-Dimensional Graphene-

Based Aerogel Embedding TiO_2 Nanoparticles and Loading MoS_2 Nanosheets as Co-Catalyst. *Int. J. Hydrogen Energy* **2014**, *39*, 19502−19512.
(4) Zhang, B.; Fan, T.; Xie, N.; Nie, G.; Zhang, H. Versatile Applications of Metal Single-Atom@2D Material Nanoplatforms. *Adv. Sci.* **2019**, *6*, 1901787.
(5) Yoshida, Y.; Izumi, Y. Recent Advances in the Preferential Thermal-/Photo-Oxidation of Carbon Monoxide: Noble Versus Inexpensive Metals and Their Reaction Mechanisms. *Catal. Surv. Asia* **2016**, *20*, 141−166.
(6) Valente, A.; Iribarren, D.; Dufour, J. Life Cycle Sustainability Assessment of Hydrogen from Biomass Gasification: A Comparison with Conventional Hydrogen. *Int. J. Hydrogen Energy* **2019**, *44*, 21193−21203.
(7) Iqbal, M. Z.; Siddique, S. Recent Progress in Efficiency of Hydrogen Evolution Process Based Photoelectrochemical Cell. *Int. J. Hydrogen Energy* **2018**, *43*, 21502−21523.
(8) Jain, N.; Roy, A.; Nair, S. Reduced $SrTiO_3$-Supported Pt-Cu Alloy Nanoparticles for Preferential Oxidation of CO in Excess Hydrogen. *Nanoscale* **2019**, *11*, 22423−22431.
(9) Ahmed, S.; Krumpelt, M. Hydrogen from Hydrocarbon Fuels for Fuel Cells. *Int. J. Hydrogen Energy* **2001**, *26*, 291−301.
(10) Montini, T.; Melchionna, M.; Monai, M.; Fornasiero, P. Fundamentals and Catalytic Applications of CeO_2-Based Materials. *Chem. Rev.* **2016**, *116*, 5987−6041.
(11) Ricken, M.; Nölting, J.; Riess, I. Specific Heat and Phase Diagram of Nonstoichiometric Ceria (CeO_{2-X}). *J. Solid State Chem.* **1984**, *54*, 89−99.
(12) *Catalysis by Ceria and Related Materials*, 2nd ed.; Trovarelli, A., Fornasiero, P., Eds.; Catalytic Science Series 12; Imperial College Press: 2013. DOI: 10.1142/p870.
(13) Koelling, D. D.; Boring, A. M.; Wood, J. H. The Electronic Structure of CeO_2 and PrO_2. *Solid State Commun.* **1983**, *47*, 227−232.
(14) Corma, A.; Atienzar, P.; García, H.; Chane-Ching, J. Y. Hierarchically Mesostructured Doped CeO2 with Potential for Solar-Cell Use. *Nat. Mater.* **2004**, *3*, 394−397.
(15) Xie, S.; Wang, Z.; Cheng, F.; Zhang, P.; Mai, W.; Tong, Y. Ceria and Ceria-Based Nanostructured Materials for Photoenergy Applications. *Nano Energy* **2017**, *34*, 313−337.
(16) Kim, S. S.; Lee, S. J.; Hong, S. C. Effect of CeO_2 Addition to Rh/Al_2O_3 Catalyst on N_2O Decomposition. *Chem. Eng. J.* **2011**, *169*, 173−179.
(17) Giordano, F.; Trovarelli, A.; De Leitenburg, C.; Giona, M. A Model for the Temperature-Programmed Reduction of Low and High Surface Area Ceria. *J. Catal.* **2000**, *193*, 273−282.
(18) Hu, S.; Zhou, F.; Wang, L.; Zhang, J. Preparation of Cu_2O/CeO_2 Heterojunction Photocatalyst for the Degradation of Acid Orange under Visible Light Irradiation. *Catal. Commun.* **2011**, *12*, 794−797.
(19) Li, L.; Yan, B. CeO_2-Bi_2O_3 Nanocomposite: Two Step Synthesis, Microstructure and Photocatalytic Activity. *J. Non-Cryst. Solids* **2009**, *355*, 776−779.
(20) Jiang, B.; Zhang, S.; Guo, X.; Jin, B.; Tian, Y. Preparation and Photocatalytic Activity of CeO_2/TiO_2 Interface Composite Film. *Appl. Surf. Sci.* **2009**, *255*, 5975−5978.
(21) Fang, J.; Bi, X.; Si, D.; Jiang, Z.; Huang, W. Spectroscopic Studies of Interfacial Structures of CeO_2 -TiO_2 Mixed Oxides. *Appl. Surf. Sci.* **2007**, *253*, 8952−8961.
(22) Karunakaran, C.; Gomathisankar, P. Solvothermal Synthesis of CeO_2-TiO_2 Nanocomposite for Visible Light Photocatalytic Detoxification of Cyanide. *ACS Sustainable Chem. Eng.* **2013**, *1*, 1555−1563.
(23) Moretti, E.; Storaro, L.; Talon, A.; Lenarda, M.; Riello, P.; Frattini, R.; de Yuso, M. V. M.; Jiménez-López, A.; Rodríguez-Castellón, E.; Ternero, F.; Caballero, A.; Holgado, J. P. Effect of Thermal Treatments on the Catalytic Behaviour in the CO Preferential Oxidation of a CuO-CeO_2-ZrO_2 Catalyst with a Flower-like Morphology. *Appl. Catal., B* **2011**, *102*, 627−637.
(24) Moretti, E.; Lenarda, M.; Riello, P.; Storaro, L.; Talon, A.; Frattini, R.; Reyes-Carmona, A.; Jiménez-López, A.; Rodríguez-Castellón, E. Influence of Synthesis Parameters on the Performance of CeO_2-CuO and CeO_2-ZrO_2-CuO Systems in the Catalytic Oxidation of CO in Excess of Hydrogen. *Appl. Catal., B* **2013**, *129*, 556−565.
(25) Moretti, E.; Storaro, L.; Talon, A.; Riello, P.; Molina, A. I.; Rodríguez-Castellón, E. 3-D Flower like Ce-Zr-Cu Mixed Oxide Systems in the CO Preferential Oxidation (CO-PROX): Effect of Catalyst Composition. *Appl. Catal., B* **2015**, *168−169*, 385−395.
(26) Furube, A.; Hashimoto, S. Insight into Plasmonic Hot-Electron Transfer and Plasmon Molecular Drive: New Dimensions in Energy Conversion and Nanofabrication. *NPG Asia Mater.* **2017**, *9*, No. e454.
(27) Ishida, T.; Murayama, T.; Taketoshi, A.; Haruta, M. Importance of Size and Contact Structure of Gold Nanoparticles for the Genesis of Unique Catalytic Processes. *Chem. Rev.* **2020**, *120*, 464−525.
(28) Hutchings, G. J. Heterogeneous Gold Catalysis. *ACS Cent. Sci.* **2018**, *4*, 1095−1101.
(29) Gellé, A.; Moores, A. Plasmonic Nanoparticles: Photocatalysts with a Bright Future. *Current Opinion in Green and Sustainable Chemistry* **2019**, *15*, 60−66.
(30) Moon, S. Y.; Song, H. C.; Gwag, E. H.; Nedrygailov, I. I.; Lee, C.; Kim, J. J.; Doh, W. H.; Park, J. Y. Plasmonic Hot Carrier-Driven Oxygen Evolution Reaction on Au Nanoparticles/TiO_2 Nanotube Arrays. *Nanoscale* **2018**, *10*, 22180−22188.
(31) Ma, X. C.; Dai, Y.; Yu, L.; Huang, B. B. Energy Transfer in Plasmonic Photocatalytic Composites. *Light: Sci. Appl.* **2016**, *5*, e16017.
(32) Liu, Z.; Hou, W.; Pavaskar, P.; Aykol, M.; Cronin, S. B. Plasmon Resonant Enhancement of Photocatalytic Water Splitting Under Visible Illumination. *Nano Lett.* **2011**, *11*, 1111−1116.
(33) Rodríguez-Aguado, E.; Infantes-Molina, A.; Talon, A.; Storaro, L.; León-Reina, L.; Rodríguez-Castellón, E.; Moretti, E. Au Nanoparticles Supported on Nanorod-like TiO_2 as Catalysts in the CO-PROX Reaction under Dark and Light Irradiation: Effect of Acidic and Alkaline Synthesis Conditions. *Int. J. Hydrogen Energy* **2019**, *44*, 923−936.
(34) Arango-Díaz, A.; Moretti, E.; Talon, A.; Storaro, L.; Lenarda, M.; Núñez, P.; Marrero-Jerez, J.; Jiménez-Jiménez, J.; Jiménez-López, A.; Rodríguez-Castellón, E. Preferential CO Oxidation (CO-PROX) Catalyzed by CuO Supported on Nanocrystalline CeO 2 Prepared by a Freeze-Drying Method. *Appl. Catal., A* **2014**, *477*, 54−63.
(35) Moretti, E.; Storaro, L.; Talon, A.; Lenarda, M. One-Pot Mesoporous Al-Ce-Cu Oxide Systems as Catalysts for the Preferential Carbon Monoxide Oxidation (CO-PROX). *Catal. Commun.* **2009**, *10*, 522−527.
(36) Jobbágy, M.; Sorbello, C.; Sileo, E. E. Crystalline Ce(III)-La(III) Double Basic Carbonates: A Chemical Shortcut to Obtain Nanometric La(III)-Doped Ceria. *J. Phys. Chem. C* **2009**, *113*, 10853−10857.
(37) Zhang, Y.; Li, Z.; Wen, X.; Liu, Y. Partial Oxidation of Methane over Ni/Ce-Ti-O Catalysts. *Chem. Eng. J.* **2006**, *121*, 115−123.
(38) Rouquerol, J.; Rouquerol, F.; Llewellyn, P.; Maurin, G.; Sing, K. S. W. *Adsorption by Powders and Porous Solids: Principles, Methodology and Applications*, 2nd ed.; Elsevier Inc.: 2013.
(39) Reddy, B. M.; Khan, A. Nanosized CeO2-SiO2, CeO2-TiO2, and CeO_2-ZrO_2 Mixed Oxides: Influence of Supporting Oxide on Thermal Stability and Oxygen Storage Properties of Ceria. *Catal. Surv. Asia* **2005**, *9*, 155−171.
(40) Oku, M.; Wagatsuma, K.; Kohiki, S. Ti 2p and Ti 3p X-Ray Photoelectron Spectra for TiO_2, SrTiO3 and BaTiO3. *Phys. Chem. Chem. Phys.* **1999**, *1*, 5327−5331.
(41) Moretti, E.; Storaro, L.; Talon, A.; Moreno-Tost, R.; Rodríguez-Castellón, E.; Jiménez-López, A.; Lenarda, M. CO Preferential Oxidation Activity of CuO/CeO_2 Supported on Zirconium Doped Mesoporous MSU Type Silica. *Catal. Lett.* **2009**, *129*, 323−330.
(42) Bêche, E.; Charvin, P.; Perarnau, D.; Abanades, S.; Flamant, G. Ce 3d XPS Investigation of Cerium Oxides and Mixed Cerium Oxide ($Ce_xTi_yO_z$). *Surf. Interface Anal.* **2008**, *40*, 264−267.
(43) Sheerin, E.; Reddy, G. K.; Smirniotis, P. Evaluation of Rh/$Ce_xTi_{1-x}O_2$ Catalysts for Synthesis of Oxygenates from Syngas Using XPS and TPR Techniques. *Catal. Today* **2016**, *263*, 75−83.
(44) Kumar, S.; Kim, Y. J.; Koo, B. H.; Lee, C. G. Structural and Magnetic Properties of Ni Doped CeO $_2$ Nanoparticles. *J. Nanosci. Nanotechnol.* **2010**, *10*, 7204−7207.

(45) Stoch, J.; Lercher, J.; Ceckiewicz, S. Correlations between XPS Binding Energies and Composition of Aluminasilicate and Phosphate Molecular Sieves. *Zeolites* **1992**, *12*, 81−85.
(46) Chahal, S.; Singh, S.; Kumar, A.; Kumar, P. Oxygen-Deficient Lanthanum Doped Cerium Oxide Nanoparticles for Potential Applications in Spintronics and Photocatalysis. *Vacuum* **2020**, *177*, 109395.
(47) Hernández, J. A.; Gómez, S. A.; Zepeda, T. A.; Fierro-González, J. C.; Fuentes, G. A. Insight into the Deactivation of Au/CeO_2 Catalysts Studied by In Situ Spectroscopy during the CO-PROX Reaction. *ACS Catal.* **2015**, *5*, 4003−4012.
(48) Deng, X.-Q.; Zhu, B.; Li, X.-S.; Liu, J.-L.; Zhu, X.; Zhu, A.-M. Visible-Light Photocatalytic Oxidation of CO over Plasmonic Au/TiO_2: Unusual Features of Oxygen Plasma Activation. *Appl. Catal., B* **2016**, *188*, 48−55.
(49) Escamilla-Perea, L.; Nava, R.; Pawelec, B.; Rosmaninho, M. G.; Peza-Ledesma, C. L.; Fierro, J. L. G. SBA-15-Supported Gold Nanoparticles Decorated by CeO_2: Structural Characteristics and CO Oxidation Activity. *Appl. Catal., A* **2010**, *381*, 42−53.
(50) Minicò, S.; Scirè, S.; Crisafulli, C.; Visco, A. M.; Galvagno, S. FT-IR Study of Au/Fe_2O_3 Catalysts for CO Oxidation at Low Temperature. *Catal. Lett.* **1997**, *47*, 273−276.
(51) Moretti, E.; Molina, A. I.; Sponchia, G.; Talon, A.; Frattini, R.; Rodriguez-Castellon, E.; Storaro, L. Low-Temperature Carbon Monoxide Oxidation over Zirconia-Supported CuO−CeO_2 catalysts: Effect of Zirconia Support Properties. *Appl. Surf. Sci.* **2017**, *403*, 612−622.
(52) Li, Y.; Sun, Q.; Kong, M.; Shi, W.; Huang, J.; Tang, J.; Zhao, X. Coupling Oxygen Ion Conduction to Photocatalysis in Mesoporous Nanorod-like Ceria Significantly Improves Photocatalytic Efficiency. *J. Phys. Chem. C* **2011**, *115*, 14050−14057.
(53) Johnston-Peck, A. C.; Senanayake, S. D.; Plata, J. J.; Kundu, S.; Xu, W.; Barrio, L.; Graciani, J.; Sanz, J. F.; Navarro, R. M.; Fierro, J. L. G.; Stach, E. A.; Rodriguez, J. A. Nature of the Mixed-Oxide Interface in Ceria-Titania Catalysts: Clusters, Chains, and Nanoparticles. *J. Phys. Chem. C* **2013**, *117*, 14463−14471.
(54) Barrio, L.; Zhou, G.; González, I. D.; Estrella, M.; Hanson, J.; Rodriguez, J. A.; Navarro, R. M.; Fierro, J. L. G. In Situ Characterization of Pt Catalysts Supported on Ceria Modified TiO_2 for the WGS Reaction: Influence of Ceria Loading. *Phys. Chem. Chem. Phys.* **2012**, *14*, 2192−2202.
(55) Park, J. B.; Graciani, J.; Evans, J.; Stacchiola, D.; Senanayake, S. D.; Barrio, L.; Liu, P.; Sanz, J. F.; Hrbek, J.; Rodriguez, J. A. Gold, Copper, and Platinum Nanoparticles Dispersed on CeO_x/TiO_2(110) Surfaces: High Water-Gas Shift Activity and the Nature of the Mixed-Metal Oxide at the Nanometer Level. *J. Am. Chem. Soc.* **2010**, *132*, 356−363.
(56) Kundu, S.; Ciston, J.; Senanayake, S. D.; Arena, D. A.; Fujita, E.; Stacchiola, D.; Barrio, L.; Navarro, R. M.; Fierro, J. L. G.; Rodriguez, J. A. Exploring the Structural and Electronic Properties of Pt/Ceria-Modified TiO_2 and Its Photocatalytic Activity for Water Splitting under Visible Light. *J. Phys. Chem. C* **2012**, *116*, 14062−14070.
(57) Mariño, F.; Descorme, C.; Duprez, D. Supported Base Metal Catalysts for the Preferential Oxidation of Carbon Monoxide in the Presence of Excess Hydrogen (PROX). *Appl. Catal., B* **2005**, *58*, 175−183.
(58) Mars, P.; van Krevelen, D. W. Oxidations Carried out by Means of Vanadium Oxide Catalysts. *Chem. Eng. Sci.* **1954**, *3*, 41−59.
(59) Luo, J.; Liu, Y.; Niu, Y.; Jiang, Q.; Huang, R.; Zhang, B.; Su, D. Insight into the Chemical Adsorption Properties of CO Molecules Supported on Au or Cu and Hybridized Au-CuO Nanoparticles. *Nanoscale* **2017**, *9*, 15033−15043.
(60) Haruta, M.; Yamada, N.; Kobayashi, T.; Iijima, S. Gold Catalysts Prepared by Coprecipitation for Low-Temperature Oxidation of Hydrogen and of Carbon Monoxide. *J. Catal.* **1989**, *115*, 301−309.
(61) Torres Sanchez, R. M.; Ueda, A.; Tanaka, K.; Haruta, M. Selective Oxidation of CO in Hydrogen over Gold Supported on Manganese Oxides. *J. Catal.* **1997**, *168*, 125−127.
(62) Rossignol, C.; Arrii, S.; Morfin, F.; Piccolo, L.; Caps, V.; Rousset, J. L. Selective Oxidation of CO over Model Gold-Based Catalysts in the Presence of H_2. *J. Catal.* **2005**, *230*, 476−483.
(63) Avgouropoulos, G.; Papavasiliou, J.; Tabakova, T.; Idakiev, V.; Ioannides, T. A Comparative Study of Ceria-Supported Gold and Copper Oxide Catalysts for Preferential CO Oxidation Reaction. *Chem. Eng. J.* **2006**, *124*, 41−45.
(64) Ivanova, S.; Pitchon, V.; Petit, C.; Caps, V. Support Effects in the Gold-Catalyzed Preferential Oxidation of CO. *ChemCatChem* **2010**, *2*, 556−563.
(65) Yang, K.; Huang, K.; Lin, L.; Chen, X.; Dai, W.; Fu, X. Superior Preferential Oxidation of Carbon Monoxide in Hydrogen-Rich Stream under Visible Light Irradiation over Gold Loaded Hedgehog-Shaped Titanium Dioxide Nanospheres: Identification of Copper Oxide Decoration as an Efficient Promoter. *J. Power Sources* **2015**, *284*, 194−205.
(66) Yang, K.; Li, Y.; Huang, K.; Chen, X.; Fu, X.; Dai, W. Promoted Effect of PANI on the Preferential Oxidation of CO in the Presence of H_2 over Au/TiO_2 under Visible Light Irradiation. *Int. J. Hydrogen Energy* **2014**, *39*, 18312−18325.
(67) Moretti, E.; Rodríguez-Aguado, E.; Infantes-Molina, A.; Rodríguez-Castellón, E.; Talon, A.; Storaro, L. Sustainable Photo-Assisted CO Oxidation in H_2-Rich Stream by Simulated Solar Light Response of Au Nanoparticles Supported on TiO_2. *Catal. Today* **2018**, *304*, 135−142.
(68) Barroso-Martín, I.; Infantes-Molina, A.; Talon, A.; Storaro, L.; Rodríguez-Aguado, E.; Rodríguez-Castellón, E.; Moretti, E. CO Preferential Photo-Oxidation in Excess of Hydrogen in Dark and Simulated Solar Light Irradiation over AuCu-Based Catalysts on SBA-15 Mesoporous Silica-Titania. *Materials* **2018**, *11*, 1203.

https://dx.doi.org/10.1021/acsami.0c08258
ACS Appl. Mater. Interfaces 2020, 12, 38019−38030